Front. Energy 2021, 15(3): 744–751
https://doi.org/10.1007/s11708-021-0775-7

RESEARCH ARTICLE

Jing BAI, Bo ZHANG, Jinhua LI, Baoxue ZHOU

Photoelectrocatalytic generation of H_2 and S from toxic H_2S by using a novel BiOI/WO_3 nanoflake array photoanode

Abstract In this paper, a photoelectrocatalytic (PEC) recovery of toxic H_2S into H_2 and S system was proposed using a novel bismuth oxyiodide (BiOI)/ tungsten trioxide (WO_3) nano-flake arrays (NFA) photoanode. The BiOI/WO_3 NFA with a vertically aligned nanostructure were uniformly prepared on the conductive substrate via transformation of tungstate following an impregnating hydroxylation of BiI_3. Compared to pure WO_3 NFA, the BiOI/WO_3 NFA promotes a significant increase of photocurrent by 200%. Owing to the excellent stability and photoactivity of the BiOI/WO_3 NFA photoanode and I^-/I_3^- catalytic system, the PEC system toward splitting of H_2S totally converted S^{2-} into S without any polysulfide (S_x^{n-}) under solar-light irradiation. Moreover, H_2 was simultaneously generated at a rate of about 0.867 mL/(h ·cm). The proposed PEC H_2S splitting system provides an efficient and sustainable route to recover H_2 and S.

Keywords bismuth oxyiodide (BiOI)/ tungsten trioxide (WO_3) nano-flake arrays (NFA), photoelectrocatalytic (PEC), H_2S splitting, H_2, S

Received Apr. 3, 2021; accepted Jun. 23, 2021; online Sept. 10, 2021

Jing BAI, Bo ZHANG, Jinhua LI
School of Environmental Science and Engineering, Shanghai Jiao Tong University, Shanghai 200240, China

Baoxue ZHOU (✉)
School of Environmental Science and Engineering, Shanghai Jiao Tong University, Shanghai 200240, China; Shanghai Institute of Pollution Control and Ecological Security, Shanghai 200090, China; Key Laboratory of Thin Film and Microfabrication Technology, Shanghai Jiao Tong University, Shanghai 200240, China
E-mail: zhoubaoxue@sjtu.edu.cn

Special Issue—Photocatalysis: From Solar Light to Hydrogen Energy (Guest Editors: Wenfeng SHANGGUAN, Akihiko KUDO, Zhi JIANG, Yuichi YAMAGUCHI)

1 Introduction

It has become a global consensus to reduce greenhouse gas emissions to control climate change. However, achieving this goal requires a significant increase in clean energy to replace the use of fossil energy. Hydrogen, as a promising green energy in the past decades, has been widely used, but the production of hydrogen in a green and cheap way still poses certain challenges. Solar hydrogen production is considered to be the most environmentally friendly way to produce hydrogen. The development of various photocatalysts to directly split water to produce hydrogen has always been an important research goal of the majority of researchers. However, direct decomposition of water to produce hydrogen faces the dilemma that few photocatalyst own a proper band structure to meet water oxidation potential and good visible light absorption at the same time. In fact, some hydrogen-rich substances can replace water as proton donors, making photocatalytic hydrogen production more efficient. For example, H_2S is an abundant chemical by-product from petroleum, natural gas, and coal gasification industries as well as naturally emanated from the putrefaction of organic substances or wastewater treatment plants, etc [1–3]. However, H_2S is also a potentially valuable chemical because H_2 and elemental sulfur S could be extracted [4]. Traditional processing techniques of H_2S, such as the Claus process, could only obtain elemental sulfur. Therefore, the hydrogen contained in H_2S is wasted. Actually, the thermodynamic decomposition of H_2S is only 33 kJ/mol (ΔG^0) within the oxidation capacity of most photoanode material [5]. Compared with the energy required to split water (ΔG^0 = 273 kJ/mol), the energy required for decomposition of H_2S is significantly lower. Therefore, developing an environmentally friendly, sustainable, and economical way of recovering H_2 and S from H_2S was highly reasonable and desirable.

Over the decade, semiconductor photoelectrocatalysis

has attracted a lot of attentions because it facilitates the utilization of sunlight to produce renewable energy and treat pollutants through an eco-friendly route [6–10]. Owing to the lower oxidation potential of H_2S, the photoelectrocatalytic (PEC) technology presents a potential to treat H_2S and recover H_2 and S simultaneously. Recently, tungsten trioxide (WO_3) nanoplates have been reported as promising photoanode materials [11] and a PEC-H_2S splitting system has been constructed based on the WO_3 phtonaode [12]. Although WO_3 has a remarkable catalytic activity, the efficiency of PEC-H_2S splitting system is still limited because WO_3 has a large band gap (about 3.0 eV) that hinders the absorption of sunlight in a small region (< 450 nm). Furthermore, the photoinduced electrons and holes still face the rapid recombination that finally lowers the quantum efficiency. To overcome these limitations, using the semiconductors ($BiVO_4$, g-C_3N_4, TiO_2, $CdWO_4$, Ag_3PO_4, etc.) coupled with WO_3 to form a heterojunction has been approved to improve the electron transportation and thus photoactivity [13–17]. However, these semiconductors have a relatively wide band gap (about 2.4–3.2 eV) which cannot remarkably enhance the absorption of visible light. Bismuth oxyiodide (BiOI) is a p-type semiconductor with a narrow band gap of 1.9 eV, which expands the absorption of visible light to 650 nm [18–20]. As reported by Odling and Robertson [21], BiOI sensitized TiO_2 films has a significant wider light absorption range from UV to visible light. Therefore, by combining the BiOI with WO_3, the absorption of visible light could be greatly enhanced and most importantly, a p–n heterojunction is formed at WO_3-BiOI interface, which builds an internal electric field for a better separation and lifetimes of photogenerated charge-carrier. Luo et al. [22] and Feng et al. [23] studied the WO_3-BiOI nanoparticle photocatalyst for the promoted visible light photocatalytic activity, respectively. However, in a PEC H_2S recovery system, a large-scale and economical preparation of BiOI-WO_3 photoelectrode material is urgently required.

In this paper, a PEC recovery of toxic H_2S into S and H_2 system was proposed by using a novel BiOI/WO_3 nanoflake arrays (NFA) photoanode combined with a I^-/I_3^- electrolyte. The vertically aligned BiOI/WO_3 NFA films were prepared via a facile, controllable, and scalable method. In comparison with bare WO_3 NFA, the photocurrent of the BiOI/WO_3 NFA increased by 200%. In the designed PEC system, H_2S was totally oxidized into element sulfur S without any polysulfide (S_x^{n-}) since I_3^- ions are gentle oxidizers [24–26]. The evaluation of the system toward splitting of H_2S under solar-light irradiation showed a good efficiency and stability during a long-term operation. High generation rates of H_2 and S (up to about 0.867 mL/(h·cm) and 1.12 mg/(h·cm)), were obtained respectively. Overall, the PEC system could provide an efficient way to splitting H_2S into H_2 and S.

2 Experimental section

2.1 Preparation of WO_3 NFA

The WO_3 NFA photoanode was fabricated using a modified chemical bath method as previously reported [11]. First, 0.4 g of $Na_2WO_4 \cdot 2H_2O$ and 0.15 g of $(NH_4)_2C_2O_4$ were dissolved in 33 mL of deionized water. Then, HCl (9 mL, w(HCl) = 37%, w is mass fraction), H_2O_2 (8 mL, $w(H_2O_2)$ = 37%, w is mass fraction), and ethanol (30 mL) were subsequently added to this solution with a strong agitation for obtaining the precursor solution. Next, the fluorine-doped tin oxide (FTO) glass (13 Ω/cm; 40 mm × 60 mm) was dipped into the solution at a constant temperature and then cooled naturally. After that, the sample was annealed at 500°C in air for 2 h. Finally, the sample was cut into two 20 mm × 60 mm pieces, one for control and the other for the fabrication of BiOI/WO_3 NFA.

2.2 Synthesis of BiOI/WO_3 NFA photoanode

BiOI was deposited onto the WO_3 NFA by using an impregnating hydroxylation method [27]. Typically, 0.94 g of BiI_3 was mixed with 2 drops of HCl (w(HCl) = 35%, w is mass fraction) in 20 mL of absolute ethanol solutions. The WO_3 NFA photoanode was then immersed into the prepared solution for 30 min and then dried in an oven at 80°C for 1 h. Subsequently, the WO_3 NFA photoanode was immersed in distilled water, and BiOI/WO_3 NFA photoanode was finally prepared by hydroxylation of BiI_3.

2.3 Characterization

The surface morphology of the prepared samples was investigated by scanning electron microscope (SEM) using a microscope equipped with an energy-dispersive X-ray (EDX) spectrometer (Ultra Plus, Zeiss, Germany). An X-ray diffraction (XRD) were performed for the crystalline phases of the samples (Rigaku D-Max B). The composition of BiOI/WO_3 NFA sample was analyzed with an ESCALAB250 X-ray photoelectron spectroscopy (XPS) measuring system. The UV-Vis spectra was conducted in a spectrophotometer (TU-1901, Pgeneral, China) using an integrating sphere.

2.4 Photoelectrochemical measurements

The photocurrent of the BiOI/WO_3 NFA photoanode was measured in a three electrode system (the NFA as the working electrode, platinum foil as the counter electrode and the NFA as the working electrode and Ag/AgCl electrode as the reference). The electrolyte was a 0.1 mol/L Na_2SO_4 solution. The current-voltage characteristics of the

samples were measured by Linear Sweep Voltammetry (LSV) at a scan rate of 50 mV/s (CHI 660c, CH Instruments Inc. USA). A 300 W xenon lamp (Perfect Light, China) was used as simulated light source (at a calibrated light intensity of 100 mW/cm^2).

2.5 PEC splitting of H_2S

Customized PEC cell with a proton membrane was applied for the H_2S splitting. The nanostructured BiOI/WO_3 NFA photoanode was put in the anodic chamber while the Pt photocathode in the cathodic chamber. The anodic compartment contained 100 mL of 0.1 mol/L Na_2SO_4 and certain amount of KI. The cathodic compartment contained 100 mL of 0.1 mol/L Na_2SO_4. Before operation, the pH of anodic solution and cathodic solution were adjusted to 1 (Fig. S7). H_2S was injected into the anodic chamber following a filtration process for S collection. Meanwhile, H_2 was measured by an online gas system (Bofeilai Technology) connected with a gas chromatograph (GC9790, Fuli, China).

3 Results and discussion

3.1 Characterization of BiOI/WO_3 NFA

The top-view and cross-section SEM images of pure WO_3 NFA and BiOI/WO_3 NFA were investigated as shown in Fig. 1. As can be seen in Figs. 1(a) and 1(b), the WO_3 film tightly adheres to the FTO substrate, showing a homogeneous flake-like morphology with a thickness of about 850 nm. The formation mechanism of WO_3 NFA proposed here can be described as Eqs. (1)–(4): the precipitation of tungstic acid first forms peroxotungstates and then after further reduction uniform and ordered $WO_3 \cdot H_2O$ films was formed. Finally, the WO_3 film was obtained via a calcination. This direct growth strategy may benefit the smaller resistance between the WO_3 film and the FTO substrate via eliminating their grain boundaries, thus resulting in a higher PEC performance.

$$WO_4^{2-} + 2H^+ \rightleftharpoons H_2WO_4 \downarrow, \quad (1)$$

$$H_2WO_4 + H_2O_2 \rightleftharpoons \text{peroxotungstates} + H_2O, \quad (2)$$

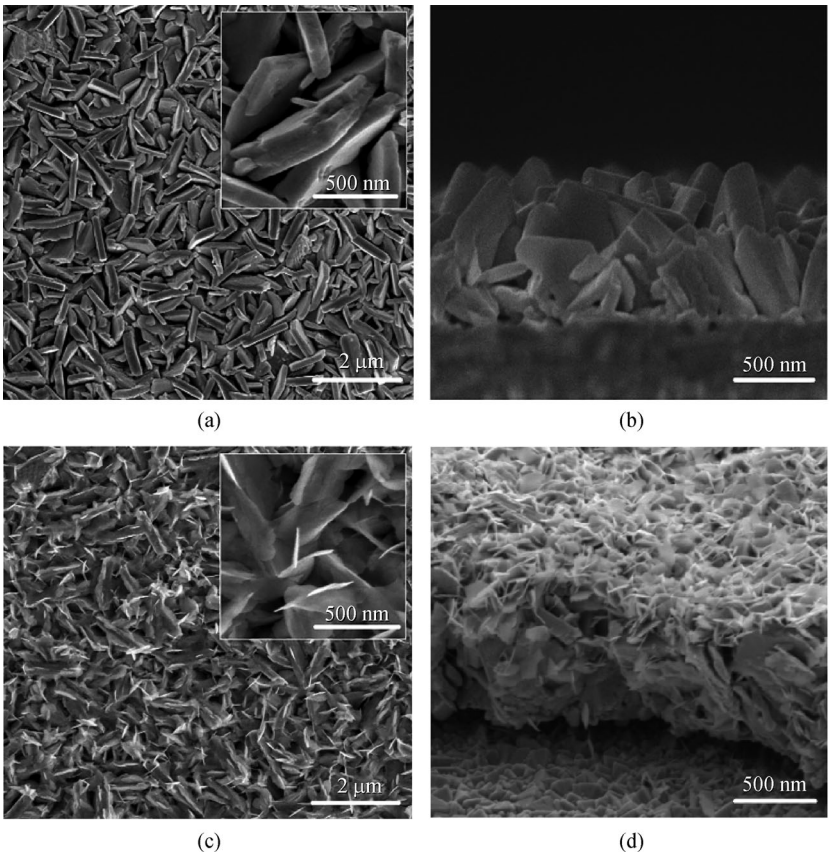

Fig. 1 SEM images of WO_3 NFA and BiOI/WO_3 NFA.
(a) Top view of WO_3 NFA; (b) cross-section of WO_3 NFA; (c) top view of BiOI/WO_3 NFA; (d) cross-section of BiOI/WO_3 NFA.

$$\text{peroxotungstates} + \text{ethanol} + H^+ \rightleftharpoons$$

$$WO_3 \cdot H_2O \downarrow + \text{aldehyde}, \quad (3)$$

$$WO_3 \cdot H_2O \rightarrow WO_3 + H_2O. \quad (4)$$

After deposition of BiOI NFA, the morphology of the sample revealed that the BiOI NFA homogenously distributes both on the surface and interstice of WO_3 NFA (Figs. 1(c) and 1(d)). The heterojunction film has a larger thickness and surface area. It can further load more BiOI on the WO_3 surface but the performance is relatively decreased possibly because the thicker BiOI film ineffectively injects charges into the WO_3 conduction band (Fig. S1).

The elemental composition of BiOI/WO_3 was investigated via an EDX detection spectrometer. As demonstrated in Fig. S2, only W, O, Bi, and I elements appear in the sample. Figure 2 exhibits the XRD patterns of the as-synthesized BiOI, WO_3, and BiOI/WO_3, respectively. The sharp and intense diffraction peaks of the samples imply that all the photocatalysts are well crystallized. The XRD pattern of pure WO_3 shows diffraction peaks at 23.1°, 23.5°, 24.3°, 28.6°, 33.5°, and 34.2°, which are in good agreement with the (002), (020), (200), (–112), (–202), and (202) diffraction planes of the orthorhombic crystalline phase of WO_3 (JCPDS Card No.43-1035). It is worth noting that the peak for monoclinic WO_3 (002) facet has a relatively low intensity, suggesting that the (002) direction is parallel to the substrate, whereas the (200) direction is vertical to the substrate owing to the intensified (200) diffraction peak. On the other hand, pure BiOI displays four distinct diffraction peaks at 29.6°, 31.6°, and 45.4°, corresponding to (102), (110), and (200) diffraction planes of the tetragonal phase of BiOI (JCPDS Card No.10-0445). Compared with pure the WO_3 and BiOI film, the BiOI/WO_3 film possesses all these peaks, implying the formation of the heterojunction. In addition, the additional peaks at 26.4°and 37.6° for all samples indicate the FTO substrate.

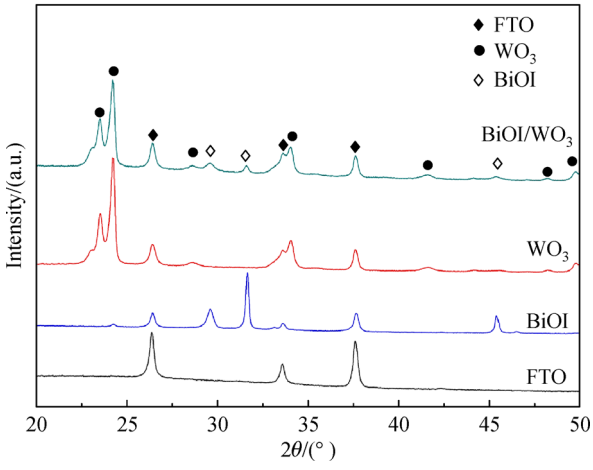

Fig. 2 XRD patterns of FTO, WO_3, BiOI, and BiOI/WO_3 electrode.

To identify the valence states of the BiOI/WO_3 sample, the XPS spectrum are illustrated in Fig. 3. The full spectrum reveals the presence of W, O, Bi, and I and no obvious impurities could be found on the surface of BiOI/WO_3 NFA (Fig. 3(a)). The O 1s (Fig. 3(a)) at the peak of 531.0 eV is assigned to the lattice oxygen of the Bi–O or W–O chemical bonding in the BiOI or WO_3 [23,28]. Figure 3(b) presents the narrow scans of Bi 4f, where two distinct peaks can be detected. The fitting peaks at 159.9 eV and 165.2 eV are assigned to Bi $4f_{7/2}$ and Bi $4f_{5/2}$ respectively, indicating the presence of Bi^{3+}. Moreover, I^- is identified by the other two distinct peaks located at 631.1 eV and 619.8 eV in Fig. 3(c) which are assigned to binding energy of I $3d_{3/2}$ and I $3d_{5/2}$ respectively. The four peaks indicate the presence of Bi^{3+} and I^- in BiOI [29]. Accordingly, Fig. 3(d) shows two strong peaks at 35.9 eV and 37.9 eV, which are assigned to W $4f_{7/2}$ and W $4f_{5/2}$ in WO_3, respectively [30]. The combined results of FE-SEM, XRD, and XPS convincingly prove the formation of BiOI/WO_3 NFA heterojunction. Based on the UV-Vis absorption spectra in Fig. 4, the absorption band edge of the pure WO_3 lies at below 475 nm owing to the intrinsic band gap of WO_3, whereas BiOI/WO_3 expands the absorption band edge to around 650 nm, presenting a stronger and broader absorption of the visible light. The band gap energy of WO_3 and BiOI is estimated to be about 2.60 eV and 1.88 eV, respectively, which are in good agreement with those reported in Refs. [22,23]. (Fig. 4(b)).

Figure 5 presents the LSV characteristics of the WO_3 and BiOI/WO_3 under illumination of chopped AM 1.5 G, respectively. A comparison of the bare WO_3 with a photocurrent density of 0.58 mA/cm^2 (0.6 V versus Ag/AgCl) clearly reveals that the WO_3 modified with BiOI shows a significant enhancement in photocurrent density of approximately 1.19 mA/cm^2 (0.6 V versus Ag/AgCl), reaching about 2 times the photocurrent of the bare WO_3 film. The semicircle radii (r) of the EIS Nyquist plot follow the order of $r(WO_3) > r(BiOI/WO_3)$, characterizing the decrease of impedance after the modification of BiOI on WO_3 (Fig. S3). The degradation of methylene blue (MB) using the BiOI/WO_3 under visible light irradiation also demonstrates the enhanced photocatalytic activities (Fig. S4). Figure 5(b) shows the schematic diagram of energy bands between the BiOI and WO_3 under visible-light irradiation. As can be seen, the highly efficient separation of photogenerated electrons and holes should be attributed to the internal electrostatic field in the p–n junction formed between BiOI and WO_3, which restrains the recombination of photogenerated electrons and holes. An external electrostatic field can further enhance the hole transfer from the semiconductor to electrolyte as well as the electron diffusion to the back contact. Therefore, the

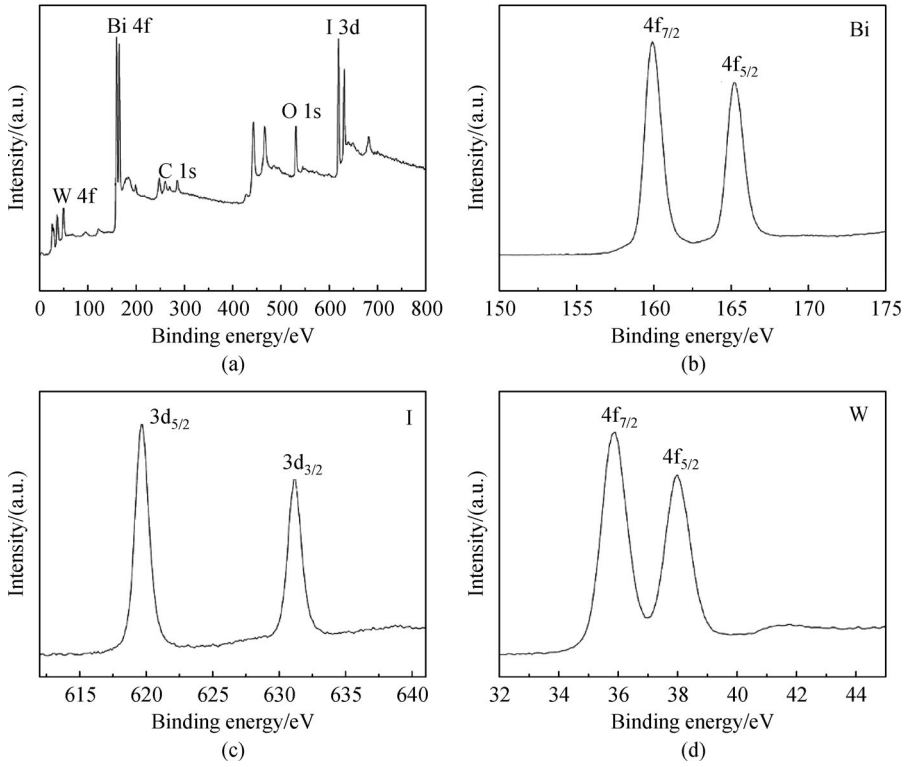

Fig. 3 X-ray photoelectron spectroscopy survey scan for BiOI/WO_3 NFA.
(a) Full spectra; (b) Bi 4f spectra; (c) I 3d spectra; (d) W 4f spectra.

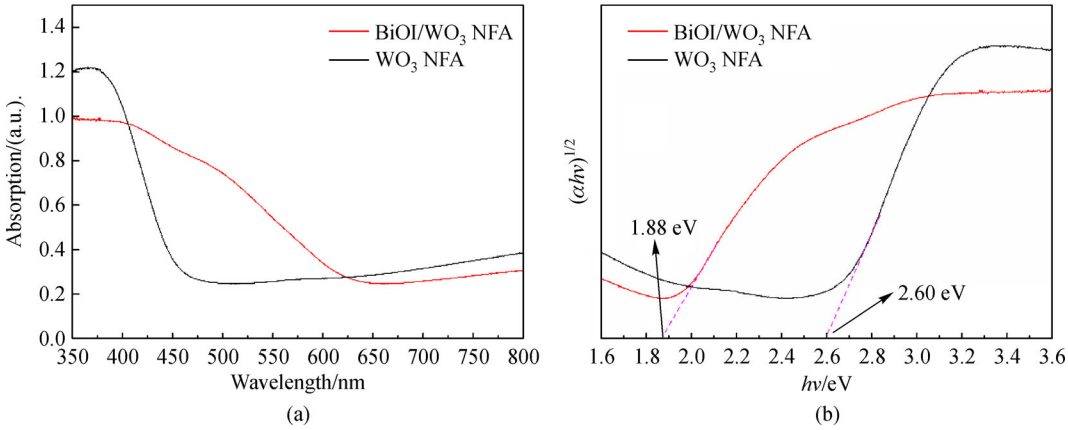

Fig. 4 UV-Vis absorption spectra.
(a) WO_3 and BiOI/WO_3 NFA; (b) band gap energy of WO_3 and BiOI/WO_3 NFA.

synergetic effects of both the internal and external electric fields realize the highest photocurrent density.

3.2 PEC splitting of H_2S

The BiOI/WO_3 NFA was then used in the PEC generation of elemental hydrogen and sulfur from H_2S. As is known, hydroxyl radical ($E^0 \approx 3.2$ V versus normal hydrogen electrode (NHE)) or photoholes ($E^0 = 2.81$ V versus NHE) induced by most semiconductor photocatalysts commonly make direct oxidation of S^{2-} into S_x^{n-} because of the high oxidation potential. Thus, only a clarifying S_x^{n-} solution with a typical yellow color can be obtained. To further confirm the existence of S_x^{n-}, a qualitative analysis was conducted through the reaction of the yellow clarifying solution with the hydrochloric acid. As can be seen in Fig. S5, the appearance of milky-white turbid demonstrates the formation of suspending S, indicating the existence of S_x^{n-}.

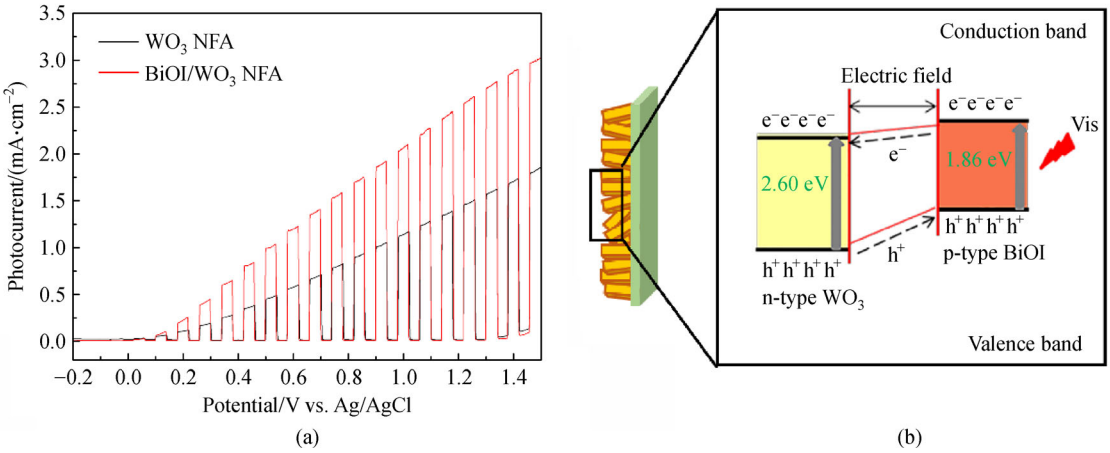

Fig. 5 Photo-response and energy bands of BiOI/WO_3NFA.
(a) LSV characteristics of WO_3 NFA and BiOI/WO_3 NFA under illumination of chopped AM 1.5 G; (b) schematic diagrams for energy bands matching in BiOI/WO_3 NFA.

In this case, a mild oxidant seems to be necessary in order to selectively convert S^{2-} into S. Herein, I^- ion was introduced into the anodic chamber in the PEC cell where I^- ions can be first oxidized into I_3^- ions by BiOI/WO_3 NFA. Since I_3^- ions only have an oxidation potential of 0.54 V (versus SHE), H_2S was favorably oxidized into S and H^+ (Eqs. (5)–(7)). Accordingly, I^- ions were recovered again for the next cycle.

$$\text{Photoanode} + h\nu \rightarrow e^- + h^+, \tag{5}$$

$$3I^- + 2h^+ \rightarrow I_3^-, \tag{6}$$

$$I_3^- + H_2S \rightarrow 3I^- + 2H^+ + S\downarrow. \tag{7}$$

The photocurrent of the system was first investigated in the existence of I^- ions. As displayed in Fig. 6, without addition of KI, the photocurrent gradually decreases from 1.2 mA/cm^2 to 0.4 mA/cm^2 during the 1000 s mainly due to the weak stability of BiOI. However, the photocurrent has a tendency to increase with the gradual increase of KI concentration and most importantly, at 200 s reaches a stable value of about 1.8 mA/cm^2 at 0.2 mol/L KI. The significant enhancement in photocurrent and stability confirms that I^- ions promote the separation of electron-hole pairs and stabilize the BiOI in a long-term operation as well.

Figure 7(a) presents the schematic of the PEC H_2S splitting system in which the BiOI/WO_3 NFA photoanode and Pt cathode are assembled in the anodic chamber and the cathodic chamber respectively and separated with a proton exchange membrane (PEM). The device was illuminated with 100 mW/cm^2 intensity and operated at a voltage of 0.6 V. During the operation, I^- ions was oxidized into I_3^- ions which further quickly reacted with S^{2-} to transform the latter into elemental S. Meanwhile, H^+ was reduced into H_2

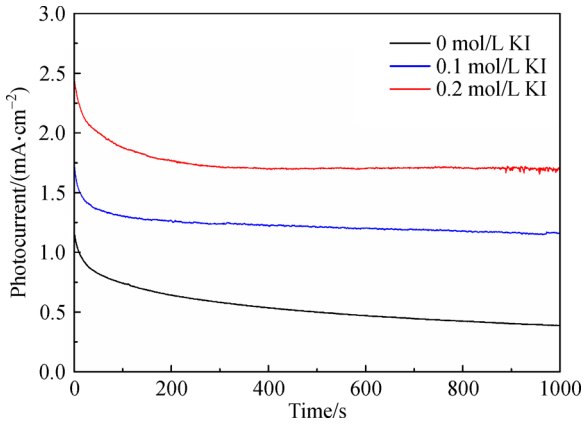

Fig. 6 Photocurrent-time (*I-t*) curves of BiOI/WO_3 NFA with different concentrations of KI. (Condition: bias potential 0.6 V, 0.1 mol/L Na_2SO_4)

gas in the cathodic chamber. Due to the continuous transition of I^-/I_3^- pairs, the H_2S could be continuously transformed to H_2 and S as $H_2S \rightarrow H_2\uparrow + S\downarrow$.

Figure 7(b) depicts the photocurrent and the corresponding color change of the electrolyte when H_2S is continuously injected into the anodic chamber. In the beginning, the photocurrent reached 1.8 mA/cm^2 and the bubbles of H_2 was observed in the cathodic chamber. Meanwhile, the color of the solution gradually changed from transparent to light yellow and then turned to bright red due to the formation of I_3^-. Then, the red solution quickly changed to a nepheloid yellowish once H_2S was injected into the anodic chamber (Fig. 7(b)). This phenomenon approved the formation of elemental S because of its bigger density and insolubilization in water. After a continuing filtration, the colorless and transparent solution was obtained again. After a long-term

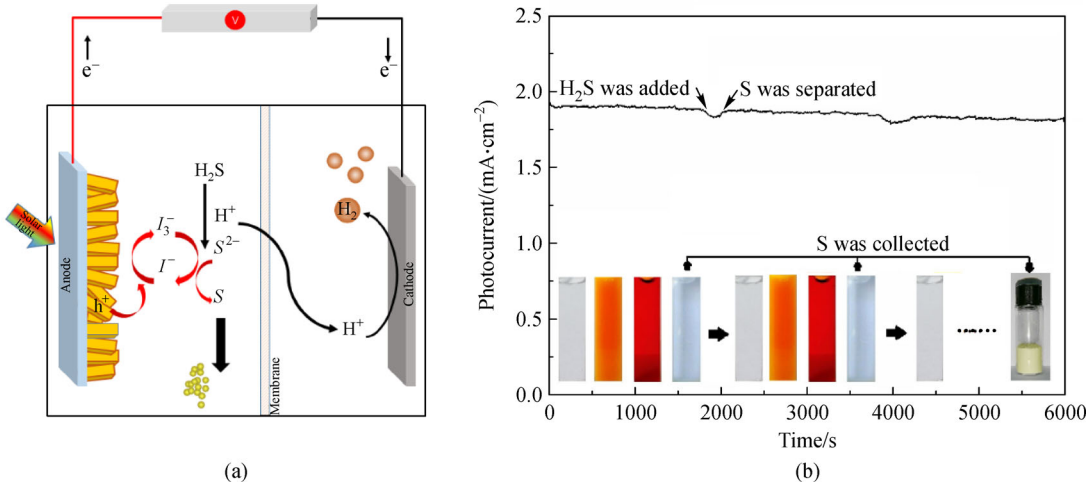

Fig. 7 PEC splitting of H_2S for H_2 and S recovery.
(a) Schematic of the PEC H_2S splitting device; (b) change of current during the operation of the system; inset: color change of the solution in anodic chamber and collected sulfur powder. (Condition: bias potential 0.6 V, 0.1 mol/L Na_2SO_4, pH 1)

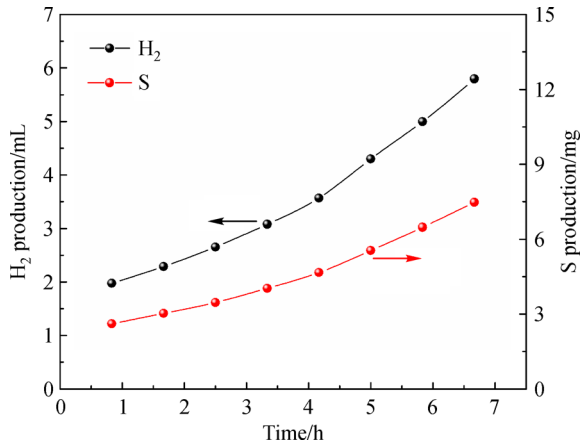

Fig. 8 Production of hydrogen and sulfur in a long-term operation. (Condition: bias potential 0.6 V, 0.1 mol/L Na_2SO_4, pH 1)

operation, much substantial S powder was collected. It is also found that the photocurrent was kept at 1.8 mA/cm^2 except a little drop with the injection of H_2S into solution. The ion ratio of I^-/I_3^- in the operation of the system gradually changed during the conversion of I^- ions to I_3^- ions at the initial time (Fig. S6). When H_2S was introduced into the anodic chamber, H_2S reacted with I_3^- ions which subsequently turned back to I^- ions, and S was produced simultaneously. The operation ran into the second cycle immediately (Fig. S5) and the concentration ratio between I^- and I_3^- presented a dynamic equilibrium.

The H^+ originated from H_2S was transferred to the cathodic chamber and reduced to the hydrogen gas finally. Figure 8 shows the production rate of H_2 and S after 7 h continuous collection. It can be seen that the production rate of H_2 and S is kept at about 0.867 mL/(h·cm) and 1.12 mg/(h·cm), respectively. Moreover, the result also indicates that the PEC-H_2S splitting system has a good stability and reusability (Fig. S8). Compared to the previous work [12], the production rate for both H_2 and S is increased by almost 2.6 times.

4 Conclusions

A novel method to prepare visible-light response BiOI/WO_3 NFA photoelectrode were demonstrated and successfully applied to PEC H_2S splitting for H_2 gas and sulfur generation. The BiOI/WO_3 NFA was studied by SEM, XRD, XPS, and EDX to analyze its physical and chemical characterization. The photoelectrochemical measurement also indicated an improved photocurrent of 2.5 mA/cm^2 compared to bare WO_3 under visible light illumination. Based on the novel photoelectrode, a PEC-H_2S splitting system was designed and showed an excellent performance of H_2S recovery into H_2 and S. The novel PEC-H_2S splitting system offers a promising H_2S recovery route for green energy generation.

Acknowledgements This work was supported by the National Key Research and Development Program of China (Nos. 2018YFE0122300 and 2018YFB1502001), Shanghai International Science and Technology Cooperation Fund Project (No. 18520744900), and the SJTU-AMED.

Electronic Supplementary Material Supplementary material is available in the online version of this article at https://doi.org/10.1007/s11708-021-0775-7 and is accessible for authorized users.

References

1. Yoosuk B, Wongsanga T, Prasassarakich P. CO_2 and H_2S binary sorption on polyamine modified fumed silica. Fuel, 2016, 168: 47–

53
2. Nunnally T, Gutsol K, Rabinovich A, et al. Dissociation of H_2S in non-equilibrium gliding arc "tornado" discharge. International Journal of Hydrogen Energy, 2009, 34(18): 7618–7625
3. Rabbani K A, Charles W, Kayaalp A, et al. Pilot-scale biofilter for the simultaneous removal of hydrogen sulphide and ammonia at a wastewater treatment plant. Biochemical Engineering Journal, 2016, 107: 1–10
4. Piéplu A, Saur O, Lavalley J C, et al. Claus catalysis and H_2S selective oxidation. Catalysis Reviews, 1998, 40(4): 409–450
5. Zong X, Chen H, Seger B, et al. Selective production of hydrogen peroxide and oxidation of hydrogen sulfide in an unbiased solar photoelectrochemical cell. Energy & Environmental Science, 2014, 7(10): 3347–3351
6. Li S, Hu S, Jiang W, et al. Facile synthesis of flower-like Ag_3VO_4/Bi_2WO_6 heterojunction with enhanced visible-light photocatalytic activity. Journal of Colloid and Interface Science, 2017, 501: 156–163
7. Wang Z, Sun H. Nanoscale in photocatalysis. Nanomaterials (Basel, Switzerland), 2017, 7(4): 86
8. Bai J, Li J, Liu Y, et al. A new glass substrate photoelectrocatalytic electrode for efficient visible-light hydrogen production: CdS sensitized TiO_2 nanotube arrays. Applied Catalysis B: Environmental, 2010, 95(3–4): 408–413
9. Liu Z, Zhang X, Nishimoto S, et al. Highly ordered TiO_2 nanotube arrays with controllable length for photoelectrocatalytic degradation of phenol. Journal of Physical Chemistry C, 2008, 112(1): 253–259
10. Wang G, Ling Y, Wheeler D A, et al. Facile synthesis of highly photoactive α-Fe_2O_3-based films for water oxidation. Nano Letters, 2011, 11(8): 3503–3509
11. Zeng Q, Li J, Bai J, et al. Preparation of vertically aligned WO_3 nanoplate array films based on peroxotungstate reduction reaction and their excellent photoelectrocatalytic performance. Applied Catalysis B: Environmental, 2017, 202: 388–396
12. Luo T, Bai J, Li J, et al. Self-driven photoelectrochemical splitting of H_2S for S and H_2 recovery and simultaneous electricity generation. Environmental Science & Technology, 2017, 51(21): 12965–12971
13. Zhang J, Yu K, Yu Y, et al. Highly effective and stable Ag_3PO_4/WO_3 photocatalysts for visible light degradation of organic dyes. Journal of Molecular Catalysis A Chemical, 2014, 391: 12–18
14. Aslam I, Cao C, Tanveer M, et al. A novel Z-scheme WO_3/$CdWO_4$ photocatalyst with enhanced visible-light photocatalytic activity for the degradation of organic pollutants. RSC Advances, 2015, 5(8): 6019–6026
15. Kim J H, Magesh G, Kang H J, et al. Carbonate-coordinated cobalt co-catalyzed $BiVO_4$/WO_3 composite photoanode tailored for CO_2 reduction to fuels. Nano Energy, 2015, 15: 153–163
16. Zhan F, Xie R, Li W, et al. *In situ* synthesis of g-C_3N_4/WO_3 heterojunction plates array films with enhanced photoelectrochemical performance. RSC Advances, 2015, 5(85): 69753–69760
17. Vargas M, Lopez D M, Murphy N R, et al. Effect of W-Ti target composition on the surface chemistry and electronic structure of WO_3-TiO_2 films made by reactive sputtering. Applied Surface Science, 2015, 353: 728–734
18. Xiao X, Zhang W. Facile synthesis of nanostructured BiOI microspheres with high visible light-induced photocatalytic activity. Journal of Materials Chemistry, 2010, 20(28): 5866
19. Dong G, Ho W, Zhang L. Photocatalytic NO removal on BiOI surface: the change from nonselective oxidation to selective oxidation. Applied Catalysis B: Environmental, 2015, 168–169: 490–496
20. Wang S, Guan Y, Wang L, et al. Fabrication of a novel bifunctional material of BiOI/Ag_3VO_4 with high adsorption-photocatalysis for efficient treatment of dye wastewater. Applied Catalysis B: Environmental, 2015, 168–169: 448–457
21. Odling G, Robertson N. SILAR BiOI-sensitized TiO_2 films for visible-light photocatalytic degradation of Rhodamine B and 4-chlorophenol. ChemPhysChem, 2017, 18(7): 728–735
22. Luo J, Zhou X, Ma L, et al. Enhanced visible-light-driven photocatalytic activity of WO_3/BiOI heterojunction photocatalysts. Journal of Molecular Catalysis A Chemical, 2015, 410: 168–176
23. Feng Y, Liu C, Che H, et al. The highly improved visible light photocatalytic activity of BiOI through fabricating a novel p–n heterojunction BiOI/WO_3 nanocomposite. CrystEngComm, 2016, 18(10): 1790–1799
24. Svensson P H, Kloo L. A vibrational spectroscopic, structural and quantum chemical study of the triiodide ion. Journal of the Chemical Society, Dalton Transactions: Inorganic Chemistry, 2000, (14): 2449–2455
25. Ejigu A, Lovelock K R J, Licence P, et al. Iodide/triiodide electrochemistry in ionic liquids: effect of viscosity on mass transport, voltammetry and scanning electrochemical microscopy. Electrochimica Acta, 2011, 56(28): 10313–10320
26. Reza-Dávila J C, Avilés-Rodríguez D, Gomez M, et al. Evaluation of antioxidant capacity by triiodide methods. ECS Transactions, 2019, 15(1): 461–469
27. Zhang X, Zhang L, Xie T, et al. Low-temperature synthesis and high visible-light-induced photocatalytic activity of BiOI/TiO_2 heterostructures. Journal of Physical Chemistry C, 2009, 113(17): 7371–7378
28. Chai B, Wang X. Enhanced visible light photocatalytic activity of BiOI/BiOCOOH composites synthesized via ion exchange strategy. RSC Advances, 2015, 5(10): 7589–7596
29. Xia J, Yin S, Li H, et al. Self-assembly and enhanced photocatalytic properties of BiOI hollow microspheres via a reactable ionic liquid. Langmuir, 2011, 27(3): 1200–1206
30. Huang L, Xu H, Li Y, et al. Visible-light-induced WO_3/g-C_3N_4 composites with enhanced photocatalytic activity. Dalton Transactions (Cambridge, England), 2013, 42(24): 8606–8616